

Abstract

A meridian scanning photometric system was designed for the simultaneous observation of the dynamic behavior of the proton and electron auroras with high time resolution. The hydrogen Balmer-beta (H_{β}) was selected as a typical emission line from proton auroras, whereas N_2^+ 4278 Å, OI 5577 Å and OI 6300 Å emissions were selected for electron auroras. The H_{β} photometer has a so-called tilting filter to measure rapid space-time variations of faint proton auroras free from the contamination of strong electron auroras. The observations were carried out from March to October 1970 at Syowa Station (corrected geomagnetic lat. -66.7° , long. 72.5°) in Antarctica. From the records of the meridian scanning photometers, spatial distributions of auroral luminosity along the geomagnetic meridian were displayed as a function of local time, and the iso-intensity contour lines were drawn. These space-time diagrams of auroral luminosity were shown to be very useful for the quantitative study of the dynamic behavior of auroras.

Using auroral space-time diagrams, the constitution of the proton and electron aurora substorms was described in detail. During the growth phase of a magnetospheric substorm, the emission zone of the proton aurora moves equatorward with a speed of 100–200 m/sec, accompanying the development of the asymmetric ring current and the positive H bay in the evening region. The equatorward movement and the growth of the asymmetric ring current were explained by an earthward movement of the ring current protons due to the intensification of the magnetospheric convection and the subsequent energization of protons through the betatron and Fermi acceleration processes. At the onset of the expansion phase, the quiet arcs suddenly brighten in the pre-midnight region, and the electron aurora bulge rapidly expands poleward and westward, whereas in the post-midnight region, the emission zone of proton auroras rapidly expands poleward and eastward with a large increase in luminosity. Proton auroras are absent in the leading edge of the expanding electron aurora bulge, while breakup-type electron auroras (arcs or bands) are not observed in the expanding proton aurora bulge. Therefore, it is suggested that there is a mechanism which accelerates electrons along the geomagnetic field lines from the magnetosphere down to the ionosphere in the pre-midnight region and protons in the post-

midnight region. After the onset of the expansion phase, the luminosity of the proton aurora greatly increases, and simultaneously the emission zone expands equatorward in the evening region, accompanying the development of the asymmetric partial ring current and the positive bay. These features can be interpreted by means of the proton injection into the trapping region due to the magnetic collapse in the tail, and the subsequent westward and earthward drift. From the relationship between the movement of the proton auroras and the geomagnetic variation, it is suggested that the positive bay in the evening hours is induced by the eastward current concentrated along the emission zone of proton auroras. The enhancement of the ionospheric conductivity due to the precipitating protons required to excite the observed proton aurora luminosity is estimated to be sufficient for the concentration of the eastward current. A close relationship between the proton aurora and the IPDP event was also observed, indicating proton pitch-angle diffusion due to the ion cyclotron waves.

Introduction

The auroral displays over the entire polar region were investigated in detail by DAVIS (1962) and AKASOFU (1963, 1964) using all-sky camera photographs obtained from a number of stations in the polar region. They indicated that these auroral displays comprise a single event which can be described in terms of the auroral substorm. In the study of the interplanetary space and the earth's magnetosphere, it is established that the auroral substorm is a manifestation of the magnetospheric substorm which is thought to be the process by which the magnetic energy stored in the magnetotail (through the interaction of the solar wind containing interplanetary magnetic fields with the magnetosphere) is explosively transformed into the kinetic energy of particles.

For the study of the generation mechanism of the magnetospheric substorm, the investigation of the auroral substorm is essential, because the auroral substorm is not only a manifestation of the magnetospheric substorm and a useful probe for investigating the behavior of the magnetospheric plasma, but it presents vital information on the dissipation of the substorm energy into the ionosphere. The magnetosphere is regarded as the region where the substorm energy is stored, whereas the ionosphere is the region where this stored energy is dissipated, and the coupling of both regions plays an essential role in the course of the magnetospheric substorm (VASYLIUNAS, 1969; OGUTI, 1971; CORONITI and KENNEL, 1972). The coupling between the magnetosphere and the ionosphere is thought to be through the field-aligned currents (ATKINSON, 1967; BOSTRÖM, 1968; SCHIELD *et al.*, 1969; AKASOFU and MENG, 1969; FUKUSHIMA, 1969; CLOUTIER *et al.*, 1970; ARMSTRONG and ZMUDA, 1970; KISABETH and ROSTOKER, 1971). The magnetospheric substorm is now suggested to consist of two phases, *i. e.*, the growth phase for a storing of the substorm energy in the magnetotail, and the expansion phase for an explosive dissipation of the stored energy into the ionosphere (McPHERRON, 1970; HONES *et al.*, 1971b; AUBRY and MCPHERRON, 1971; IIJIMA and NAGATA, 1971; CORONITI and KENNEL, 1971; MCPHERRON *et al.*, 1972).

This paper aims at studying the generation mechanism for the magnetospheric substorm from the investigation of the dynamic relationship between the

proton aurora and the electron aurora. Previous studies of the auroral substorm concentrated on the electron excited aurora. The principal reason for this is that proton auroras are much more faint compared with electron auroras (the intensity of H_{β} emissions in proton auroras is usually only 20–50R). Proton auroras are thus rarely discriminative on the all-sky camera records. Therefore, high-sensitive spectroscopic methods are required for the measurement of proton auroras. However, previous observations with spectroscopic instruments had severe limitations on the measurement of rapid temporal and spatial variations of proton auroras. The records of proton auroras with a spectrograph (for example, patrol spectrograph, MEINEL, 1951) are hardly suitable for the study of the proton aurora substorm because of the low time resolution of the instrument. The fixed filter photometer (for example, OMHOLT, 1957) increased the time resolution, but it could not eliminate the contamination at hydrogen emission lines from active electron auroras as suggested by EATHER (1967b). These disadvantages were greatly improved by EATHER and JACKA (1966) by introducing a tilting filter photometer to observe hydrogen emissions. Through a continuous tilting of the interference filter, this technique allowed one to scan hydrogen emission lines and to determine their line intensity in the presence of strong background continuum emissions. EATHER and JACKA (1966) measured H_{β} emissions as faint as 1–2R by using a tilting filter with a 3-inch diameter and 3-Å bandwidth. A tilting filter photometer is thought to be the most suitable instrument for the measurement of proton auroras.

By means of an improved tilting filter photometer mounted on a coelostat for the north-south scanning along the geomagnetic meridian, the dynamic behavior of proton auroras during magnetospheric substorms was effectively observed for the first time with a high time resolution (tilting time and north-south scanning time are 1 sec and 45 sec, respectively). The dynamic behavior of electron auroras was simultaneously observed by multicolor meridian-scanning photometers with a north-south scanning time of 5 sec. The observed emission lines are N_2^+ 4278 Å, OI 5577 Å and OI 6300 Å. The observations were carried out from March to October of 1970 at Syowa Station, Antarctica (geographic lat. 69°00'S, long. 39°35'E; corrected geomagnetic lat. –66.7°, long. 72.5°; $L=6.4$). For this period, various other observations for the upper atmosphere research were carried out simultaneously with the auroral measurement, *e. g.*, geomagnetic variations, geomagnetic micropulsations, VLF emissions, cosmic noise absorption and the vertical sounding of the ionosphere with ionosonde. The records of these observations were also utilized in this paper.

In Part I of this paper, the meridian-scanning photometric system for the observation of rapid space-time variations of proton and electron auroras is introduced, and some typical examples of the measurements with this photometric system are shown. Especially, it is demonstrated that the measurement of faint proton auroras can be easily carried out in the presence of intense electron auroras. In Part II, developing features of proton auroras and electron auroras during magnetospheric substorms are described, and a phenomenological model for

magnetospheric substorms is given. That is, in Chapter 3 of Part II, the space-time diagrams of the auroral luminosity obtained from the records of the meridian-scanning photometers are shown to be very useful for studying dynamic behavior of proton and electron auroras, and the diurnal movements of the auroral precipitation regions on quiet and disturbed days are given through the analysis of these space-time diagrams. Using the auroral space-time diagrams and the geomagnetic records from a number of auroral-zone stations, the features of proton and electron aurora substorms are described in detail in Chapter 4 for each local-time region, *i. e.*, the early evening hours (GLT 14 – 18 h), the late evening hours (GLT 18 – 22 h), the late evening–midnight hours (GLT 22 – 00 h) and the midnight–early morning hours (GLT 00 – 03 h). Chapter 5 describes the relationship between the appearance of proton auroras and the development of other phenomena closely associated with the proton auroras in the evening hours, *e. g.*, asymmetric partial ring current, positive bay and ULF emissions. Then, the worldwide developments of proton auroras and electron auroras during a magnetospheric substorm and the associated phenomena are summarized in Chapter 6 for each phase of a substorm, *i. e.*, the growth phase, the expansion phase and the recovery phase. On the basis of these developing features of the proton and electron aurora substorms, the generation mechanism of the magnetospheric substorm is discussed in Chapter 7. In this chapter, it is suggested that there is a mechanism which accelerates protons along the geomagnetic field lines from the magnetosphere to the ionosphere in the morning region and electrons in the evening region, respectively, and the onset of the expansion phase, *i. e.*, the auroral breakup takes place when a positive feedback system is formed, as a result of the development of field-aligned currents in the above mechanism. The source regions of the proton and electron auroras in the magnetosphere, the relationship between the equatorward movement of the proton auroral emission zone during the growth phase and the magnetospheric convection, and the correlation of the increase in the proton aurora luminosity during the expansion phase with the proton injection into the trapping region are also discussed in Chapter 7. The principal problems in this investigation and the future topics are mentioned in Chapter 8.

PART I
MERIDIAN-SCANNING PHOTOMETRIC SYSTEM FOR
PROTON AURORAS AND ELECTRON AURORAS

1. Instrumentation

1.1. H_{β} meridian-scanning tilting-filter photometer

A high time-resolution meridian-scanning photometer was constructed to observe the rapid time and space variations of H_{β} emissions in proton auroras. The instrument consists of a coelostat scanning from the north to the south and back again along the geomagnetic meridian and a tilting filter photometer to detect the intensities and Doppler shifts of incident H_{β} emissions.

When the normal of the multilayer interference filter is tilted by an angle θ to the incident light, the wavelength of peak transmission λ_0 shifts toward

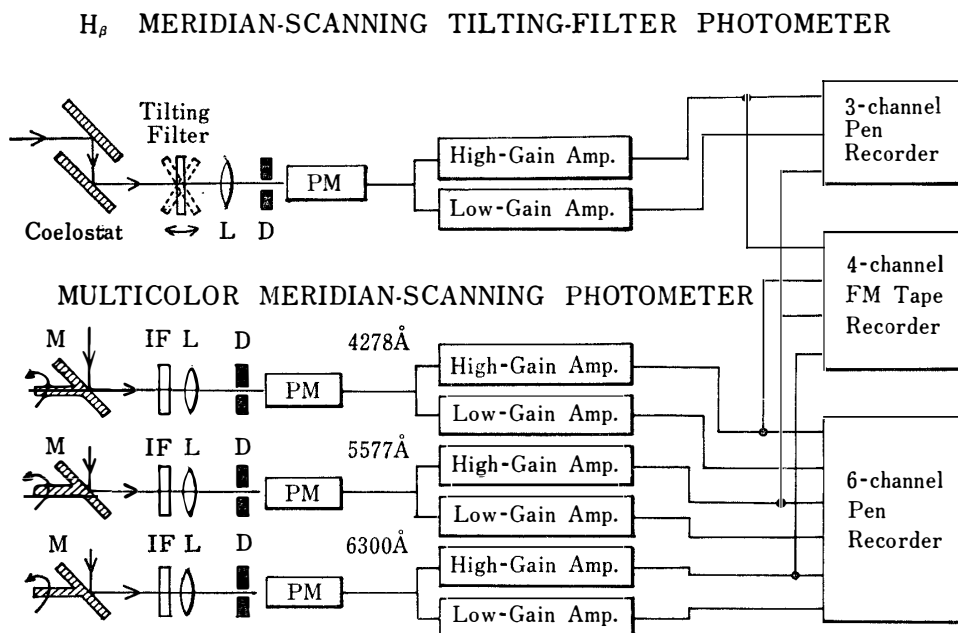


Fig. 1. Block diagram of meridian-scanning photometric system.

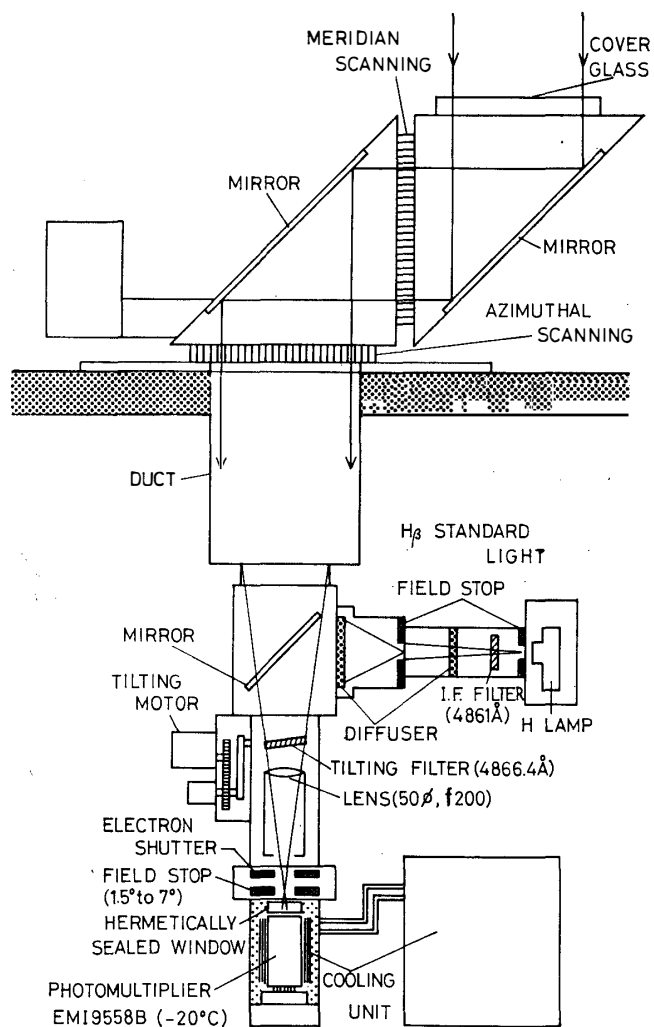


Fig. 2. Schematic diagram of H_{β} meridian-scanning tilting-filter photometer.

shorter wavelength according to the approximate formula (EATHER and REASONER, 1969),

$$\frac{\lambda_{\theta} - \lambda_0}{\lambda_0} = \frac{\delta\lambda}{\lambda_0} = -\frac{\theta^2}{2\mu^{*2}} \quad (1)$$

where μ^* is an effective refractive index of the medium between the layers.

The tilting filter photometer scans the H_{β} line by periodically tilting the narrow band pass filter. The instrument can measure the H_{β} line profile and simultaneous background emission. Through this technique H_{β} intensities can be determined in the presence of strong background radiations of electron auroras.

A schematic diagram of the instrument is given in Fig. 2. The coelostat was set up outdoors. Its north-south scanning time is 45 sec. The auroral light which

enters the telescope of the coelostat is guided into the photometer through a duct. By inclining a mirror at the top of the photometer, auroral light is cut off, and the light from H_β standard source enters the photometer for absolute calibration of the instrument.

The H_β standard light source is a hydrogen lamp whose current is accurately controlled. The light from the lamp gets through the interference filter with peak transmission wavelength at 4861 \AA , and the selected H_β line emission passes through two diffusing screens to give uniform illumination. The intensity of the H_β standard light can be varied by manual operation of the rotating field stops. Calibration of this standard light source was made by means of the L101 EOA irradiance standard (cf. Section 1.3.).

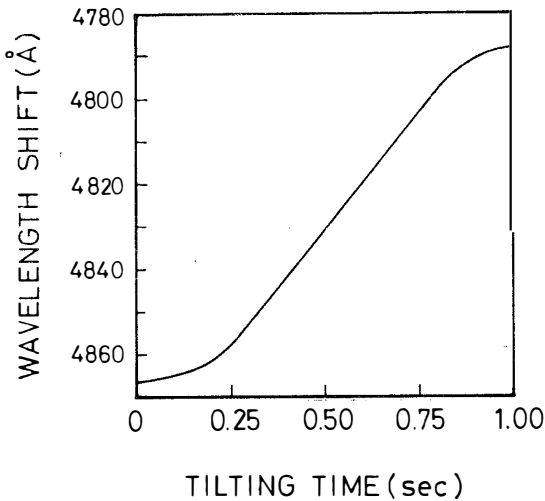


Fig. 3. Wavelength shift of peak transmission of the filter as a function of tilting time.

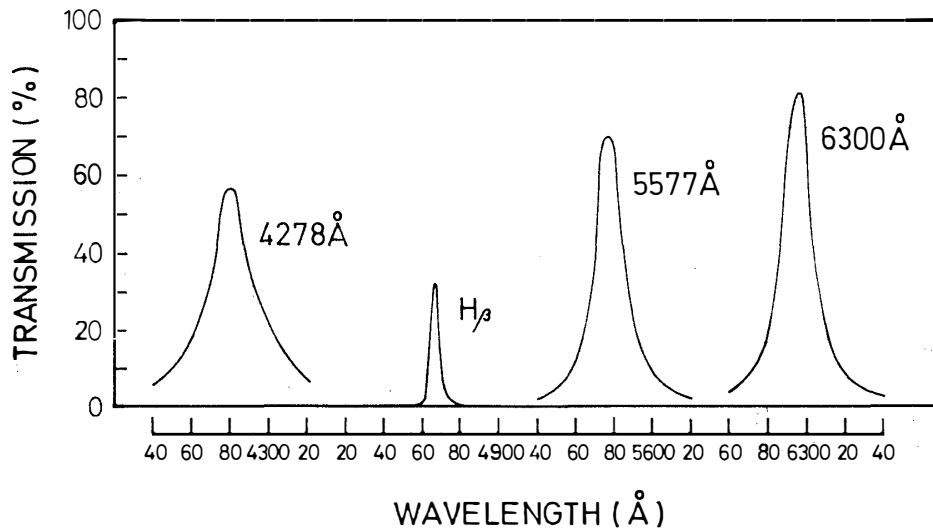


Fig. 4. Transmission curves of interference filters for N_2^+ 4278 \AA , H_β , OI 5577 \AA and OI 6300 \AA .

The interference filter tilts continuously from 0° to 15° (and back to 0°) by a synchronous motor. The tilting speed can be changed at two steps by replacing the synchronous motor. The time required for the tilt from 0° to 15° is either 1 sec or 0.25 sec, and it scans wavelengths between 4866 \AA and 4788 \AA . The shift of peak transmission wavelength with tilting time is shown in Fig. 3. The wavelength scan is linear with tilting time for the range between 4860 \AA and 4800 \AA . The interference filter used is 2 inches in diameter and has a half-power bandwidth of 2.1 \AA and peak transmission of 32 % at 4866.4 \AA (the characteristics of this filter are shown in Fig. 4 and Table 1).

Table 1. Characteristics of interference filters.

Species	Wavelength (\AA)	Transmission		Bandwidth (\AA)
		T_{max}	T_{line}	
N_2^+ I. N. G. (0, 0)	4278.1	0.62	0.60	24.0
H_β	4861.33	0.32	0.32	2.1
OI	5577.34	0.74	0.60	23.8
OI	6300.31	0.80	0.74	27.4

The H_β emission, after passing through a tilting interference filter, is focused on the field stop position by the convex lens and is defocused again on the cathode of a photomultiplier tube. The field of view can be varied from 1.5° to 7.0° by manual operation. The base line of the record can be determined by cutting off the light into a photomultiplier tube with an electric shutter. A pho-

Table 2. Photomultiplier specifications.

Type	R374-HTV	R268-HTV	9558B-EMI
Wavelength of maximum sensitivity	4200 \AA	4400 \AA	4200 \AA
Anode-cathode voltage	1000 V	1000 V	1250 V
Cathode sensitivity	120 $\mu\text{A/lumen}$	60 $\mu\text{A/lumen}$	120 $\mu\text{A/lumen}$
Anode sensitivity	50 $\mu\text{A/lumen}$	150 $\mu\text{A/lumen}$	120 $\mu\text{A/lumen}$
Current amplification	4×10^5	2.5×10^6	1×10^6
Anode dark current	0.005 μA	0.03 μA	0.002 μA
Spectral response number	S 20	S 11	S 20
Quantum efficiency	0.07 (6300 \AA)	0.15 (4278 \AA) 0.035(5577 \AA)	0.15 (4861 \AA)

tomultiplier (9558B-EMI) is mounted in the hermetically sealed box which is cooled down to about -20°C . The dark current of the photomultiplier is less than 5×10^{-11} A. Its characteristics are listed in Table 2.

The output photocurrent is amplified by the two IC operational amplifiers with different gains in order to cover a wide dynamic range of intensity. Their output signals are recorded on a 3-channel pen-recorder and a 4-channel FM data recorder (Fig. 1). The sensitivity of the photometer on the chart records is shown in Table 3. A dynamical range of 0.25 to 100 R/Å can be obtained with the present recording system.

Table 3. Sensitivity of the photometers on the pen-oscillograph chart and measurable intensity range.

Species	Sensitivity		Measurable intensity range
	High-gain	Low-gain	
N_2^+ 4278 Å	200 R/mm	2.5 kR/mm	0.1 - 100 kR
OI 5577 Å	200 R/mm	2.5 kR/mm	0.1 - 100 kR
OI 6300 Å	60 R/mm	1.0 kR/mm	0.03 - 40 kR
H_β	0.25 R/Åmm	2.5 R/Åmm	0.25 - 100 R/Å

1.2. Multicolor meridian-scanning photometers

In order to get the information about rapid temporal and spatial variations of electron auroras and energy spectra of precipitating electrons, multicolor meridian-scanning photometers were constructed. The selected emission lines are N_2^+ 4278 Å, OI 5577 Å and OI 6300 Å emissions. A schematic diagram of the photometers is shown in Fig 5.

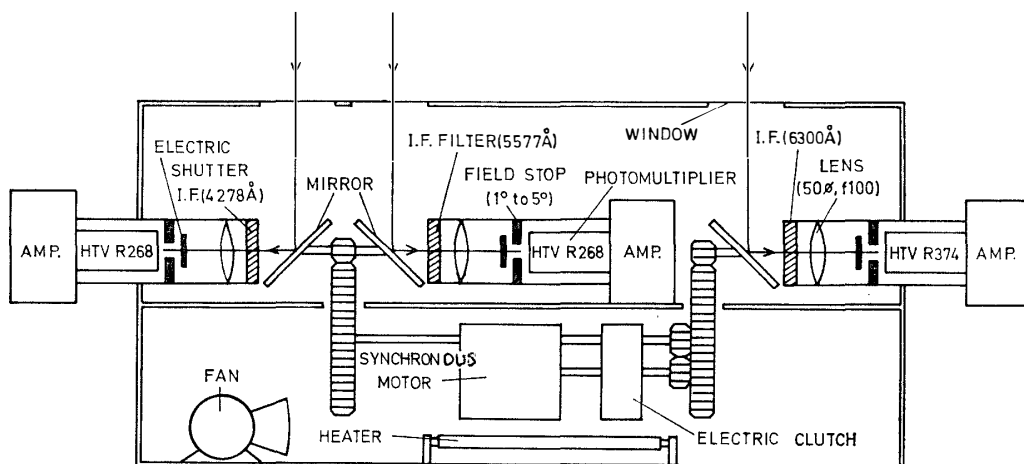


Fig. 5. Schematic diagram of multicolor meridian-scanning photometers.

The equipment consists of a chamber which houses the driving mechanisms and a chamber for the photometers. As the instrument was set up outdoors, the chamber of the driving mechanisms was air-conditioned at about +15°C with a thermo-fan, while the photometer chamber did not have any heater and was cooled down about -20°C of ambient temperature in the winter. This cooling of photometers was useful for reducing the dark current of photomultiplier.

Rotating mirrors scan from the north to the south and back again along a geomagnetic meridian. The scanning speed can be varied in two steps by altering the rotating speed of a synchronous motor, and the scanning time is either 2.5 sec or 5 sec.

The optical specifications are quite similar to that of the H_{β} photometer except that the filters are used at fixed positions. The characteristics of the interference filters are shown in Fig. 4 and Table 1. The fields of view can be selected between 1° and 5°. The photomultiplier tubes used are R 374-HTV for the detection of OI 6300 Å, and R 268-HTV for OI 5577 Å and N_2^+ 4278 Å. The dark currents are less than 0.005 and 0.03 μA , respectively. The characteristics of these photomultiplier tubes are shown in Table 2.

As the dynamic range of auroral luminosity is wide, the output photocurrents are amplified separately by high-gain and low-gain IC operational amplifiers and are registered on a 6-channel pen-recorder and a 4-channel FM data recorder (Fig. 1). The recording sensitivities are listed in Table 3. The measurable range of the intensity is 30 R to 40 kR for OI 6300 Å emissions, and 100 R to 100 kR for OI 5577 Å and N_2^+ 4278 Å emissions.

The calibration of these photometers were carried out by a standard diffuse surface illuminated by a tungsten lamp. Its brightness can be varied by changing the electric current passing through the lamp filament. The absolute brightness was calibrated by the L101 EOA irradiance standard (cf. Section 1.3).

1.3. Calibration of meridian-scanning photometers

Calibration of the photometers was performed by means of a L101 type standard light source manufactured by Electro Optics Associate. It is the point source type iodine lamp which emits a continuum spectrum in the UV through the IR range. The output signal of the photometer for the incident L101 irradiance is calculated from the following equation,

$$V_{L101} = \Phi_{L101} \cdot S \cdot W_{L101} \cdot \eta_{\lambda} \cdot e \cdot G \cdot R \cdot A \quad (2)$$

where

- V_{L101} : output voltage of the photometer (volt)
- Φ_{L101} : brightness of L101 light source (photons/cm²/sec/Å)
- S : area of object lens (cm²)
- W_{L101} : equivalent band width of interference filter (Å)
- η_{λ} : quantum efficiency of photocathode (electron/photon)
- e : electronic charge (coulomb)
- G : current amplification of photomultiplier tube

R : input resistance of electric circuit (ohm)

A : gain of amplifier

On the other hand, auroras are assumed to be a homogeneous surface source. Therefore, the output of the photometer for auroral emission is:

$$V_{AUR} = I_{AUR} \cdot S \cdot \Omega \cdot T_{AUR} \cdot \eta_{\lambda} \cdot e \cdot G \cdot R \cdot A \quad (3)$$

where

I_{AUR} : intensity of auroral emission line (photons/cm²/sec/sterad)

Ω : solid angle of field view (sterad)

T_{AUR} : transmission of interference filter

For the H_{β} tilting filter photometer, put $4\pi I_{AUR} = 2$ rayleighs = 2×10^6 photons/cm²/sec/sterad, $S = 20$ cm², $\Omega = 0.006$ sterad, $T_{AUR} = 0.32$, $\eta_{\lambda} = 0.15$, $G = 10^6$, $R = 10^7$ ohm, $A = 100$, and we have $V_{AUR} = 0.15$ volt.

The calibration constant K of the photometer is determined from the equations (2) and (3),

$$K = \frac{4\pi}{\Omega} \cdot \frac{W_{L101}}{T_{AUR}} \cdot \frac{\Phi_{L101}}{V_{L101}} \quad (\text{rayleighs/volt}) \quad (4)$$

The calibration constants of the four photometers are listed in Table 3.

1.4. Other instruments used for the upper atmosphere research

Other instruments used in the observations for the upper atmospheric physics research at Syowa Station, Antarctica were as follows:

- (a) Aurora
 - i) 35mm all-sky camera with a fish-eye lens (two frames per minute).
 - ii) Zenith photometers for the measurement of N_2^+ 4278 Å emission (5° and 30° fields of view).
 - iii) Aurora radar (carrier wave of 112.2 MHz, elevation angle of 20°).
- (b) Geomagnetism
 - i) 3-component fluxgate magnetometer.
 - ii) 3-component induction magnetometer (continuous recording of pulsations with a tape recorder and a scratch film recorder).
- (c) Ionosphere
 - i) Ionosonde for vertical sounding operated every 15 minutes.
 - ii) Riometers ($f = 10, 20, 30, 50$ and 70 MHz).
- (d) VLF emissions
 - i) Narrow-band field intensity recorders ($f = 0.3, 0.5, 0.7, 1.0, 1.4$ and 2.0 kHz for chorus emissions, and $4, 8, 14, 32, 64$ and 128 kHz for auroral hiss).
 - ii) Magnetic tape recorder for continuous recording with a tape speed of 4.75 cm/sec (frequency range of 0.2 to 5.0 kHz).
 - iii) $0.2 - 2$ kHz and $0.3 - 100$ kHz heterodyne spectrographs.
 - iv) Real-time spectral analyzer with 31 channel bandpass filters (frequency range of 0.2 to 4.0 kHz).

2. Observational Results

2.1. Some typical measurements by meridian-scanning photometers

Using the meridian-scanning photometric system, observations of proton auroras and electron auroras were carried out from March to October of 1970 at Syowa Station, Antarctica. Some examples of records are shown in Figs. 6-9.

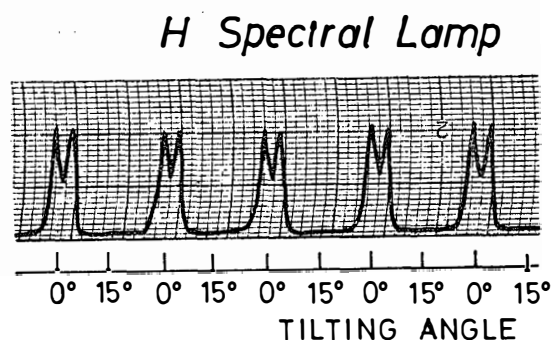


Fig. 6. Wavelength scanned profile of H_{β} standard light source with a H_{β} tilting-filter photometer.

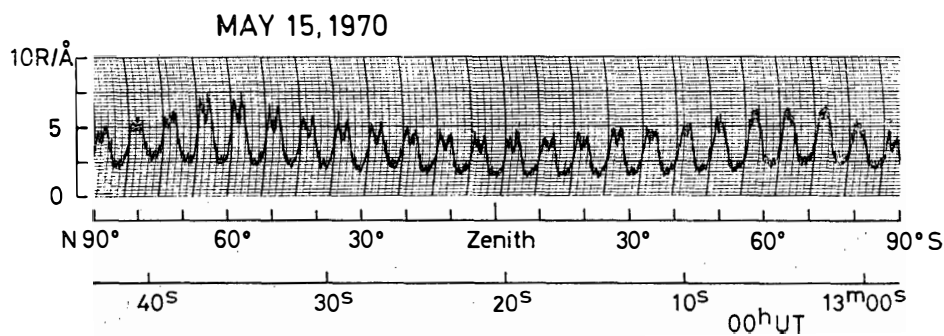


Fig. 7. Example of auroral H_{β} emission record across the sky with a H_{β} meridian-scanning tilting-filter photometer. This event was observed in the course of proton aurora breakup at the post-midnight.

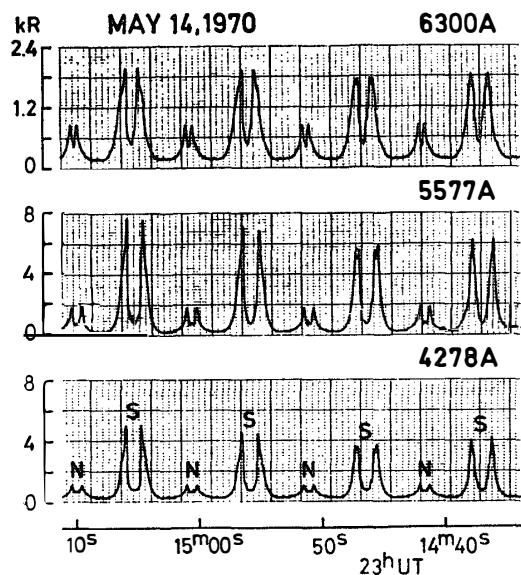


Fig. 8. Example of multicolor meridian-scanning photometer record for auroral quiet arc near the pole-side horizon.

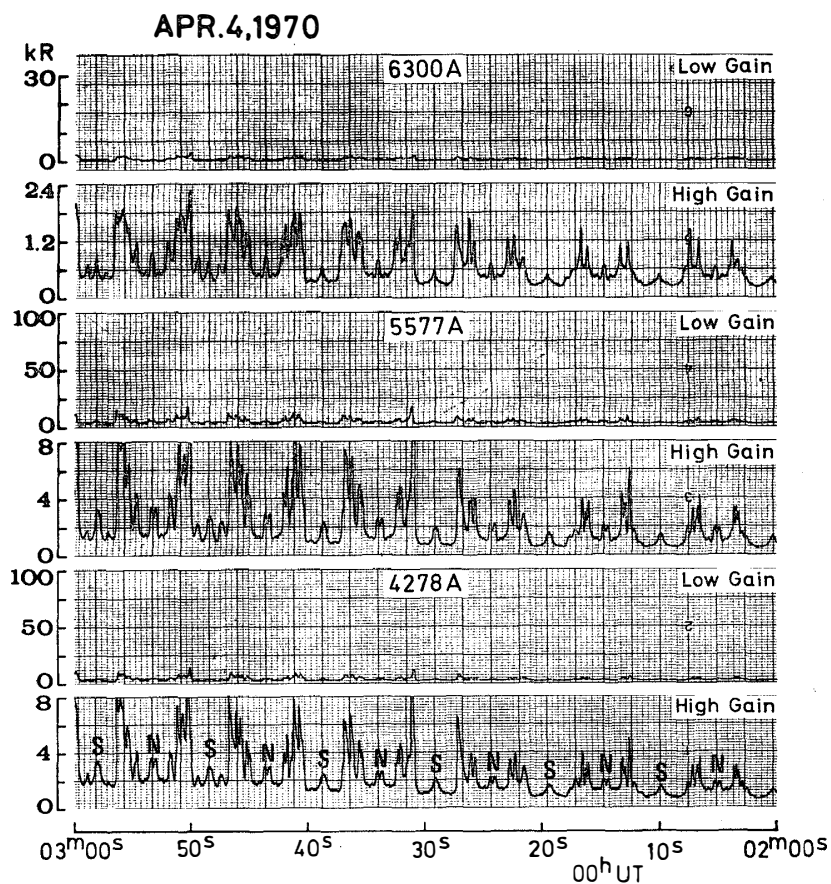


Fig. 9. Photometric traces of N_2^+ 4278 Å, OI 5577 Å and OI 6300 Å emissions at the onset of auroral breakup event.

Fig. 6 illustrates the trace for the H_β line from H_β standard light source. The wavelength of peak intensity is 4861 \AA . The finite width of the recorded profile results from the bandwidth of the interference filter. The H_β emission in proton auroras is usually Doppler-shifted by $5\text{--}7 \text{ \AA}$ and Doppler-broadened in an halfwidth of about 20 \AA (EATHER, 1967b). Fig. 7 is an example of the scan record of the H_β emission along the geomagnetic meridian during the course of the proton auroral breakup event near midnight (cf. Section 4.3.). The Doppler shift is evidently greatest for the emission from the magnetic zenith ($\sim 10^\circ\text{N}$).

The record of quiet arc near the poleward horizon by the multicolor meridian-scanning photometers is shown in Fig. 8. Fig. 9 is the record of N_2^+ 4278 \AA , OI 5577 \AA and OI 6300 \AA emissions at the onset of an auroral breakup event. The poleward expansion of their emissions can be noticed.

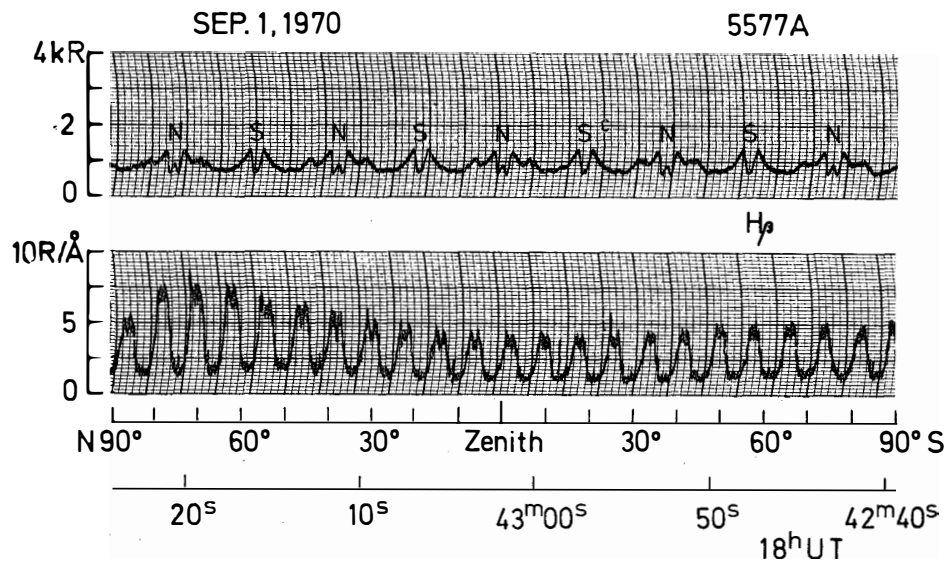


Fig. 10. Example of proton aurora without accompanying electron aurora in the evening hours.

Fig. 10 is an example of the proton aurora without accompanying electron aurora in the evening hours. The intensity of OI 5577 \AA emission is very low, and the intensity ratio of OI 5577 \AA to H_β is approximately 10. This intensity ratio is in reasonable agreement with the theoretical prediction by EATHER (1967 a) when OI 5577 \AA and H_β emissions are considered to be simultaneously excited by precipitating protons.

2.2. Measurements of faint proton auroras in the presence of active electron auroras

The proton aurora is very faint compared with the electron excited aurora. The typical values of H_β intensity observed at Syowa Station in the winter of 1970 were 20 – 50 R. The maximum value was 140 R which was observed during the main phase of the magnetic storm of September 1, 1970. Therefore, it is

important to evaluate the contamination from bright electron auroras. Fig. 11 is the example of H_β emission present with an active rayed band of electron aurora which was located near $35^\circ N$ zenith angle. The intensity of the OI 5577 emission in active rayed band is 25 kR, and the contamination from this electron aurora at H_β wavelength is 2.5 R/Å. On the other hand, the wavelength-integrated intensity of the H_β emission on the equator side of the active rayed band is

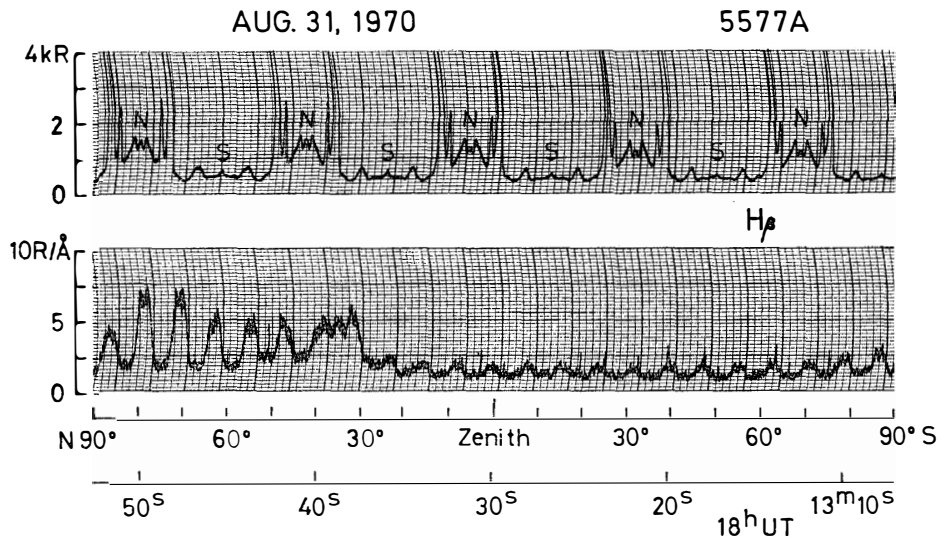


Fig. 11. Photometric traces of H_β emission lying equatorward of active rayed band of electron aurora near $35^\circ N$ zenith angle.

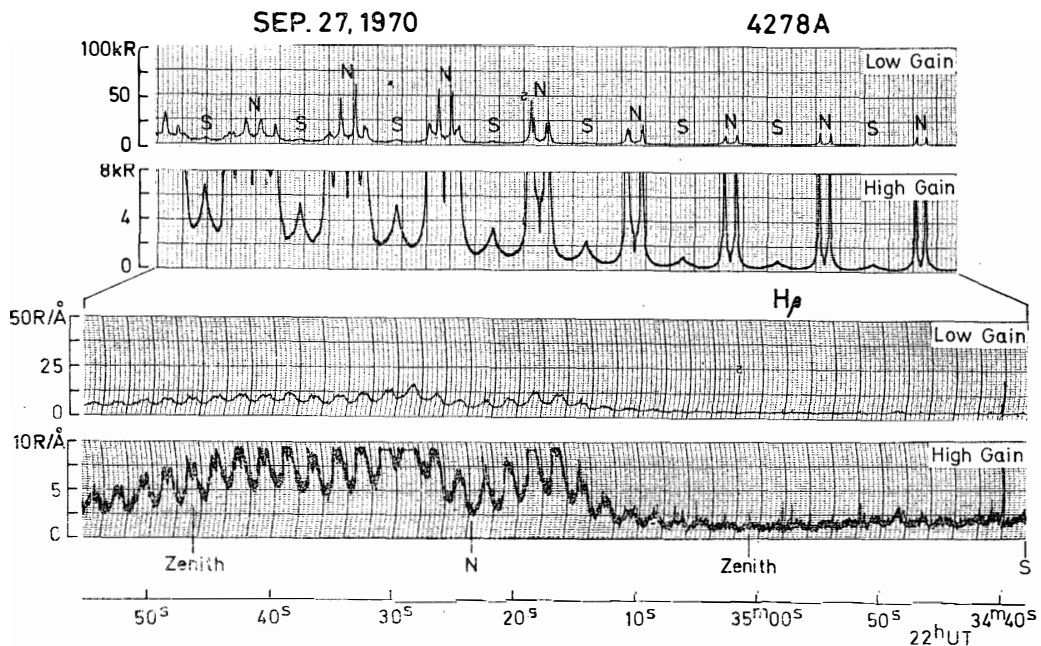


Fig. 12. Example of record for an electron auroral breakup event accompanied by a rapid enhancement of proton aurora across the sky.

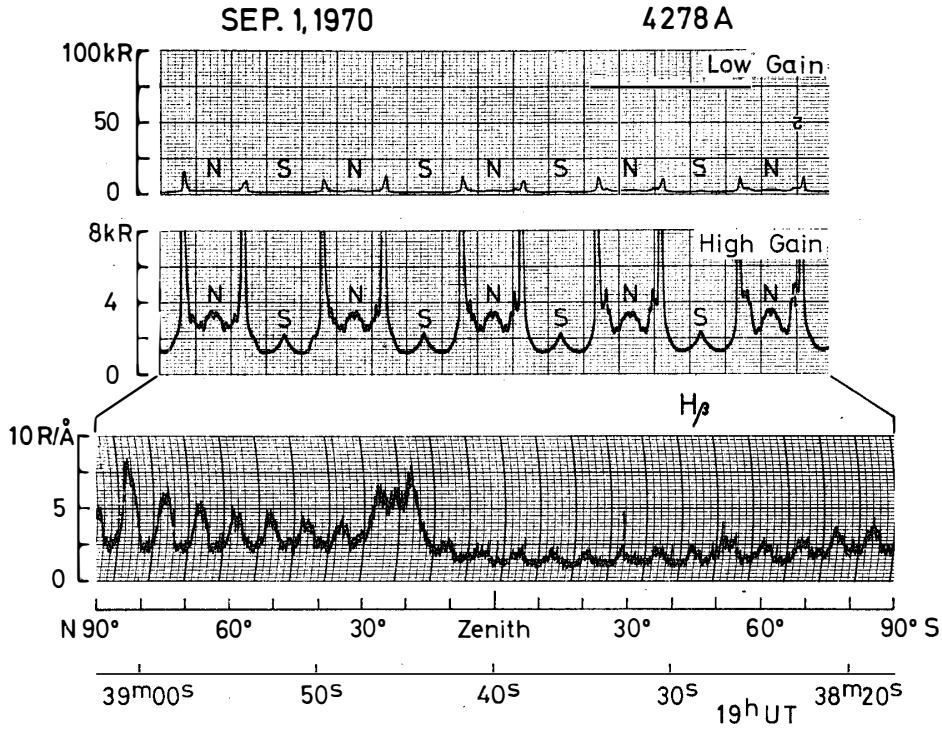


Fig. 13. Record of electron auroral breakup event in the evening hours. Breakup of electron excited aurora occurred on the pole-side of H_{β} emission zone. An enhancement of background continuum near $20^{\circ}N$ zenith angle in H_{β} emission record is due to a contamination from active band of electron aurora.

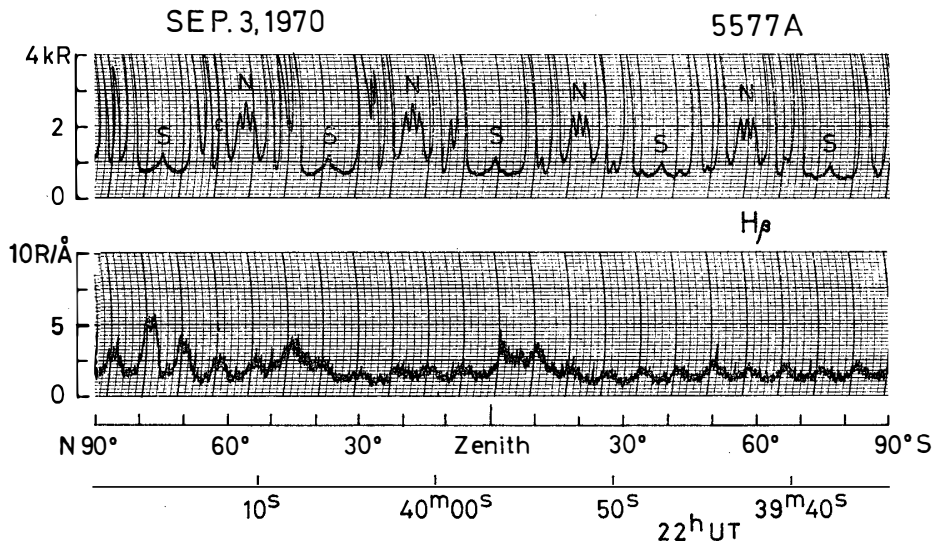


Fig. 14. Record of electron auroral breakup event in the evening hours. Event is not followed by poleward expansion of H_{β} emission zone. An enhancement of background continuum near $45^{\circ}N$ and $5^{\circ}S$ zenith angles in H_{β} emission record is due to a contamination from active rayed bands of electron aurora.

80 R. If a fixed filter photometer is used, the contamination of electron aurora cannot be separated. EATHER (1967b) concluded that a contamination from a brightness II aurora would be approximately an 80 R enhancement of the H_{β} signal, if a 40 Å bandwidth fixed filter was used. Fig. 11 shows that the emission zone of H_{β} is separated from that of active electron auroras and lies equatorward of it.

Fig. 12 is an example of the auroral breakup event accompanied by a rapid enhancement of proton aurora across the sky. The increase of background continuum by a contamination from electron auroras can be noticed after 22 h 35 m 10 s UT on the record of the H_{β} emission.

Figs. 13 and 14 are the records of breakup events of electron auroras in the evening hours. In contrast to the breakup event near midnight, the evening events are not usually followed by the poleward expansion of the H_{β} emission zone. The enhancement of background continuum near 20°N, 45°N and 5°S zenith angles in the H_{β} emission records is due to a contamination from active rayed bands of electron auroras.